LIGHTHOUSE

SWEDISH MARITIME COMPETENCE CENTRE

LIGHTHOUSE REPORTS

Pilot Study of Electric Hubless Rim-Driven Thrusters for Transport in Inland Waterways

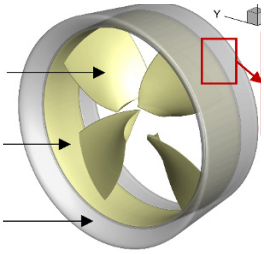

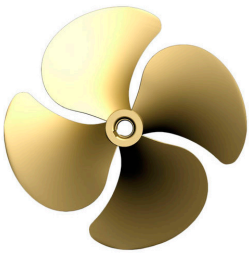

En förstudie utförd inom Trafikverkets branschprogram Hållbarsjöfart som drivs av Lighthouse. Publicerad September 2023

www.lighthouse.nu

LIGHTHOUSE
SWEDISH MARITIME COMPETENCE CENTRE

HÅLLBAR SJÖFART

Pilot Study of Electric Hubless Rim-Driven Thrusters for Transport in Inland Waterways

This project studied a conceptual hubless rim-driven thruster (RDT) in which the blades are driven by an outer rim instead of a central hub. A novel approach to enhance the hydrodynamic efficiency of this concept was suggested by altering the gap geometry, and its validity was subsequently confirmed through numerical simulations. The results of this project are valuable for the development of effective RDTs for electric vessels operating on inland waterways.

Authors
Hua-Dong Yao

In cooperation with
Alex Shiri from RISE Maritime

Fredrik Falkman from Swedish Sea Rescue Society

Fredrik von Elern from Swedish Maritime Technology Forum

Magnus Karlsson from Kongsberg Maritime

A prestudy carried out within the Swedish Transport Administration's industry program Sustainable Shipping, operated by Lighthouse

Summary

The performance of marine propellers is substantially influenced by the power transmission through the hub and gearbox. This accounts for power loss, large space usage, heavy weights, noise and vibration. In contrast to conventional propellers, the concept of hubless rim-driven thrusters (RDTs) are a radical design, whose blades are driven by an outer rim rather than a hub. The outer rim can be easily driven by electric motors. Therefore, the negative effects from the hub are reduced.

In this pilot study, a classical hubless RDT configuration was investigated to understand flow characteristics related to the gap geometry. A new approach to enhance the hydrodynamic efficiency was suggested by altering the gap geometric parameters such as its axial passage length, and its inlet and outlet oblique angles. The numerical approach was the Reynolds-averaged Navier-Stokes (RANS) equations with the k–ω shear stress transport (SST) turbulence model.

Due to the pressure increase after the main flow passes through the rotating blades, the flow inside gap was driven upstream. In other words, the gap flow direction was opposite to the main flow direction. It was found that the hydrodynamic efficiency was increased as the gap axial passage length was shortened, which was realized by increasing the oblique angle but fixing the gap inlet and outlet positions. Moving the inlet and outlet to further downstream and upstream positions had negligible effects on the hydrodynamic efficiency and led to recirculating flow within the gap near its inlet.

The findings shed light on how the gap geometry can be designed in order to improve the hydrodynamic performance of RDTs. The results of this project should be valuable for the development of effective RDTs for electric vessels operating on inland waterways.

Sammanfattning

Marinpropellrars prestanda påverkas i hög grad av kraftöverföringen genom navet och växellådan. Detta leder till effektförluster, stort utrymme, tunga vikter, buller och vibrationer. I motsats till konventionella propellrar är konceptet med elektrisk navlös thrusters (RDT) en radikal design, vars blad drivs av en yttre fälg snarare än ett nav. Den yttre kanten kan enkelt drivas av elmotorer. Därför minskar de negativa effekterna från navet.

I denna pilotstudie undersöktes en klassisk navlös RDT-konfiguration för att förstå hur flödesegenskaper är relaterade till gapgeometrin. Ett nytt tillvägagångssätt för att förbättra den hydrodynamiska effektiviteten föreslogs genom att ändra de geometriska parametrarna för gapet, såsom dess axiella passagelängd och dess inlopps- och utloppsvinklar. Den numeriska metoden var Reynolds-medelvärdet av Navier-Stokes (RANS) ekvationer med k-ω skjuvspänningstransport (SST) turbulensmodell.

På grund av tryckökningen efter att huvudflödet passerat genom de roterande bladen drevs flödet inuti gapet uppströms. Med andra ord var gapets flödesriktning motsatt huvudflödesriktningen. Det visade sig att den hydrodynamiska effektiviteten ökade när gapets axiella passagelängd förkortades, vilket uppnåddes genom att öka den sneda vinkeln men fixera positionerna för gapets inlopp och utlopp. Att flytta inloppet och utloppet till positioner längre nedströms respektive uppströms hade försumbara effekter på den hydrodynamiska effektiviteten och ledde till återcirkulerande flöde i gapet nära dess inlopp.

Resultaten kastar ljus över hur gapgeometrin kan utformas för att förbättra den hydrodynamiska prestandan hos RDT. Resultaten propellrar för elektriska fartyg som trafikerar inre vattenvägar.

Contents

1 Introduction

With the increase in international maritime transactions, there has been a daily increase in the demand for vessel capacity and propulsion power. The disadvantages of traditional marine propulsion systems have gradually become apparent. The size and power of the main engine increases with the propulsion power demand. The structural design of the propulsion shaft system is also more complex, increasing ship design difficulty and construction costs, decreasing ship space utilization, and deteriorating propulsion efficiency.

1.1 Rim-driven thruster

Traditional marine propellers are engineered with hubs that establish the connection between the propellers and turbine engines. Furthermore, in light of the fact that the engines yield high-speed and low-torque revolutions, it becomes necessary to incorporate gearboxes within the hubs themselves. This is to facilitate the conversion of the engine output into low-speed and high-torque revolutions, which are essential for the appropriate functioning of the propellers. The drawbacks associated with hubs and gearboxes encompass notable power loss resulting from the relative movement of solid surfaces, extensive engine housing requirements, considerable weight, noise and vibration, as well as the emission of greenhouse gases such as CO2 due to the utilization of fossil fuels.

The challenges inherent in the hub-driven propulsion system can be effectively addressed by implementing a rim-driven thruster (RDT). The rotational force that propels the blades of the RDT is generated through a circular rim that is firmly connected to the tips of the blades, in contrast to a conventional propeller that derives its power from its shaft (Grümmer, 2016). The blades are mounted onto the motor rotor that is a circular rim integrated with permanent magnets, and the motor stator is positioned within a duct. Since the stator and rotor components of the motor are separately assembled, they are completely immersed in water. This enables the process of cooling to occur in the space of the gap (also referred to as the clearance). Furthermore, it is not imperative to provide the RDT with water-tight treatment in regard to rotational movements.

Kort (1940) proposed the first RDT concept model in a patent. Following that, more RDT patents were put forth, but all of them focused exclusively on the description of the broad concept of the device, without addressing the design of the machine itself or its performance (Yan et al., 2017). Researchers have been exploring RDT technology a lot lately, and some of their findings have been applied to ships.

Regarding computational fluid dynamics (CFD) methods of turbulence modelling for the simulations RDTs, Dubas et al. (2015) compared re-normalisation group k–ε and k–ω Shear Stress Transport (SST) turbulence models. Their results showed that the SST k–ω model was more robust in dealing with RDT-stator interactions

at low advance ratios. Liu et al. (2022a; 2022b) simulated the effect of several transition turbulence models on the hydrodynamic performance prediction.

Gaggero (2020) established a simulation-based design optimization method that was used to improve the RDT blade shape as regards to the hydrodynamic propulsion performance and decrease cavitation. Song et al. (2020) studied a variety of factors influencing the hydrodynamic performance, including the aspect ratio of the duct, the diffusion ratio, the contraction ratio of duct, and the tip diameter ratio of the blade.

Despite the rim is used to rotate the blades, the hub can be still included in the structure of an RDT. It has been therefore interesting to understand to which extent the hub affects the hydrodynamic efficiency. Yakovlev et al. (2011) compared the open water characteristics of RDTs with and without hubs through model experiments. Cao et al. (2012) numerically analysed the case of four distinct propeller blade configurations. The simulation method was based on the Reynolds Averaged Navier–Stokes (RANS) equations, and their results revealed that the largest radial circulation of the flow occurs at the blade tip. Song et al. (2015) compared four pairs of hub-type and hubless RDTs with varied hub diameters by means of numerical simulations. They found that that hubless RDTs were more efficient than hub-type RDTs. The reason was that the hubless RDTs produced more thrust and torque but having a lower thrust ratio, which is the ratio of the blade thrust coefficient to the sum of the thrust coefficients of the the blade and duct.

1.2 Hubless concept of RDT

Unlike traditional propellers, the concept of hubless rim-driven thrusters (RDT) does not have a hub. The RDT blades are driven by assembling the blade tips onto the inner surface of the duct (i.e., the rim). In recent years, due to the quick development of advanced manufacturing technologies and electric motors, the concept becomes attractive in the marine industry.

The basic idea of designing an RDT electric motor is to construct the rim with a brushless DC motor and permanent magnet synchronous motor, which provides a wide range of motor speeds with low heat generation. A fault-tolerant permanent magnet rim has been proposed by Li, et al. (2018).

In the marine industry, Van der Velden® Marine Systems (2006) developed three RDTs with the powers of 550, 650 and 800 kW. Rolls-Royce (Bang, et al., 2008) also proposed an RDT design for a bow thrust of 800 kW. A prototype 30 kW was constructed by Tuohy, et al. (2010). Besides, in recent years, Voith has produced a variety of RDTs with a wide power range between 50-1500 kW (Voith, 2021). Kongsberg Maritime also produces RDTs (e.g., TT-PM 1600), and Yamaha Motor launched the evaluation of their RDT product (2020). Hubs are still included in their products although blades are driven by rims. This is different from the

products of Vioth as well as the designs of SSRS (Andersen, 2014; Santiago, 2019; Adler, 2020).

According to Drouen, et al., (2008), the structure of the RDT is effective to produce high thrust and emit low noise. Matching the motor and propeller characteristics was outlined as an important factor to obtain optimal performance. An optimized blade pitch distribution in the radial direction was investigated by Yakovlev, et al. (2011). Open water performance and cavitation characteristics were studied as well. Furthermore, Cao, et al. (2012) predicted the blade loadings and wake for an RDT using a steady CFD method of Reynolds averaged Navier-Stokes (RANS) equations. They found that the rim geometry is crucial for preventing the flow recirculation near the blade tip. Then, the effects of the rim geometry were studied by Cai, et al., (2015). Zhu et al. (2022) tested the external and studied the inner flow characteristics to reveal the flow loss mechanism.

1.3 Advantages of rim-driven system

Utilizing the rim as a driving mechanism for the propeller yields benefits across various dimensions, leading to its more economical effectiveness compared to traditional propellers (Lea et al., 2003).

- A compact design with reduced weight and space occupation is achieved by integrating an electric motor into the rim.
- The mechanical efficiency is increased because the transmission loss associated with the hub and the relevant accessories (seals, bearings and gearboxes) is excluded. Moreover, the maintenance of this system becomes simpler.
- The hydrodynamic efficiency is increased. As found by Lea et al. (2003), the RDT is more efficient than the conventional propeller. The efficiency does not change much under various operation conditions.
- Specific devices for cooling the motor are not needed, because the water passing the rim is efficient to transfer heat. This also leads to low power consumption.
- The noise impact to the environment is greatly reduced. The simple electric system produces much lower noise and vibration than the conventional mechanical system with the hub and gearbox. Moreover, the hydrodynamic noise generated from propeller tip vortices is eliminated because the blade tips are mounted on the rim.

As noticed, the electrified rim-driven propulsion system is beneficial to promoting electric vessels, since the rotating structure in the rim can be easily designed with highly efficient electric motors (Li et al., 2018; Lin et al., 2022). The electrical motor is designed to form the rim around the propeller. This design allows the motor to produce a higher torque at a lower RPM.

1.4 Advantages of hubless structure

Apart from the benefit brought in by the electric rim, the hubless RDT have other advantages because of the elimination of the hub, as compared to conventional propellers. For example, the damage caused by long fibers (e.g., floating fishing nets or ropes) clogged on the hub is eliminated. Therefore, the hubless RDT can be applied in complex water situations. The weight of the whole propulsion system is reduced. And the hydrodynamic loss caused by the hub is removed.

The hubless RDT concept can be generally applied to replace conventional propellers for vessels of different sizes. For example, small boats, large passenger vessels, and underwater vehicles. The concept improves the vessel performance (the efficiency and the noise pollution) and, particularly, promoting the development of electric vessels.

1.5 Previous studies on the effects of clearance

According to the above literature research, most previous studies have focused on optimizing the hydrodynamic characteristics of the propeller and duct profile of the RDT. On the other hand, the influence of the gap flow between the rotor and stator on the hydrodynamic performance cannot be ignored.

Cao et al. (2014) investigated the effects of radial and axial gap sizes on flow variables and the hydrodynamic performance based on RDT configurations with and without a propeller. The simulation results showed that enlarging the gap width increased the frictional torque coefficient on the rim surface. Liu and Vanierschot (2021) employed a moving reference frame (MRF) technique to simulate a ducted propeller and an RDT, and the gap flow was analysed. According to their study, the presence of the rim and induced gap flow introduced obvious negative effects on the hydrodynamic performance, leading to a significant reduction in the hydrodynamic efficiency compared to the ducted propeller. Zhai et al. (2022) conducted the optimization of a duct for an RDT with the consideration of the effect of the gap. The hydrodynamic characteristics of a counter-rotating RDT considering the gap flow were investigated using the RANS method (Jiang et al., 2022). It was found that due to the inclusion of the gap flow, the torque computed in the simulations deviated from the empirical formulae by more than 10%.

1.6 Scope of this study

This research was motivated by the fact that the gap flow can affect the hydrodynamic efficiency of RDTs. The aims were to understand the hydrodynamics of the RDT, in particular the gap flow structures, and to identify some critical parameters or factors affecting the gap flow and consequently the hydrodynamic efficiency. Hence, the focus was positioned on the geometric parameters near the gap inlet and outlet.

Although the existing empirical formulations in the literature are capable to predict the hydrodynamic coefficients such as thrust and torque, the influence of the gap flow has been usually omitted. As there is limited knowledge that can be transferred to the present topic, high-fidelity numerical simulations were employed to address physical details. The RANS approach with the SST k-ω turbulence model was used in the simulations. This approach is generally cheaper than advanced CFD methods such as large eddy simulation and detached eddy simulation, as have been noticed based on canonical flow cases such as rotating cylinders (Lin et al., 2020) and RDT flow (Cao et al., 2012).

2 RDT configurations

The geometry of the hubless RDT propeller was designed by modifying a conventional propeller (i.e., removing the hub, adjusting the shapes of the blade root and tip, and adding a rim with a streamlined sectional profile. The design was based on the typical MARIN 19A duct and Ka 4-70 propeller. This combination is adopted by most RDT studies (Grümmer, 2016; Jiang, 2022; Song et al., 2020). The benchmark geometry of the gap refers to the research of Liu and Vanierschot (2021). The main parameters the hubless RDT configuration are shown in Table 1. The blade area ratio (λ_a) is defined as the ratio of the developed area of all blades to the disk area ($A_0 = \pi D_b^2/4$), and the blade pitch ratio (λ_p) is defined as the ratio of the blade pitch to the blade diameter (D_b). An overview of the geometry of the configuration is shown Figure 1. The rotor and stator parts are marked out.

Table 1. The key geometry parameters of the hubless RDT configuration in this project.

	Unit	Value
Number of blades (Z)	–	4
Blade diameter (D_b)	m	0.25
Blade area ratio (λ_a)	–	0.7
Blade pitch ratio (λ_p)	–	1.0
Blade tip diameter (D_t)	m	0.05
Duct diameter (D_d)	m	0.3
Duct length (L_d)	m	0.125
Rim thickness (H)	m	0.006
Gap width (S)	m	0.0015

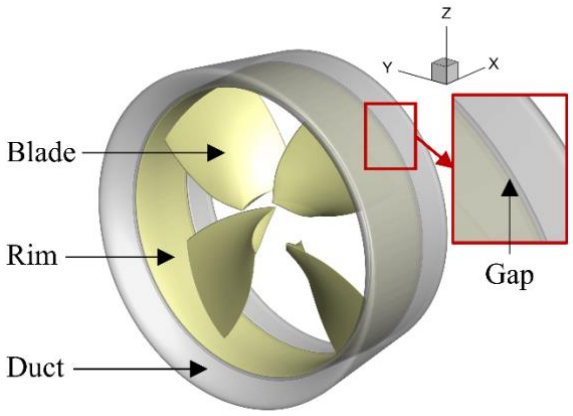

Figure 1. The geometry of the hubless RDT, where the rotor is colored yellow, and the stator is colored gray.

The geometry of the gap between the duct and rim is illustrated in Figure 2. The parameters controlling the gap geometry are highlighted. The axial segment length of the gap is L_1, and the distance between the gap inlet and outlet is L_2. The gap width (S) is kept constant. The reference values of L_1 and L_2 are equal to 0.066m.

In the RDT designs made in previous studies, the default value of oblique angle (θ) outlined in Figure 2 is equal to 90°, leading to that the inlet and outlet passages are normal to the rotation axis. In this work, θ is altered in the range from 90° to 150° so as to investigate the effect of oblique gap passages. When adjusting θ, the parameters L_1 or L_2 remain constant.

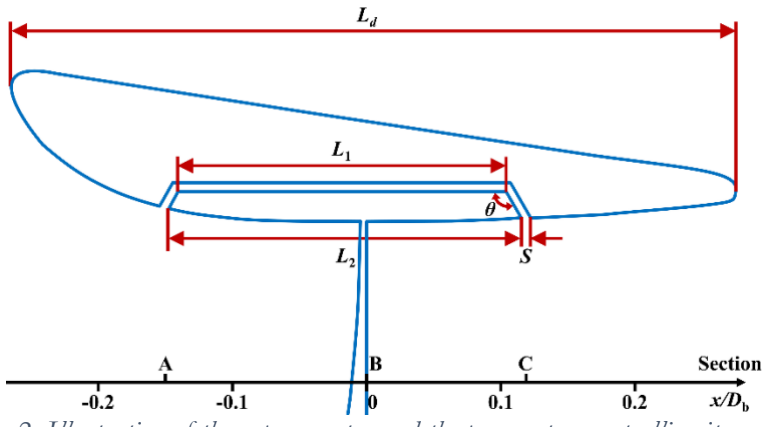

Figure 2. Illustration of the gap geometry and the parameters controlling its geometry.

2.1.1 Hydrodynamic coefficients of interest

In this project, the hydrodynamic performance was evaluated in terms of the following hydrodynamic coefficients:

$$J = V_a/(nD_b), \quad (5)$$

$$K_T = T/(\rho n^2 D_b^4), \quad (6)$$

$$K_Q = Q/(\rho n^2 D_b^5), \quad (7)$$

$$\eta = JK_T/\left(2\pi K_Q\right), \tag{8}$$

where J denotes the advance coefficient, V_a the inflow velocity, n the propeller rotation speed, K_T the thrust coefficient, T the thrust, K_Q the torque coefficient, Q the torque, and η the efficiency.

3 Method

3.1 Method of numerical simulation

The finite volume method was used in the numerical simulation, and the flow was regarded to be incompressible. The simulation tool was the open-source software OpenFOAM, and the simpleFoam module of the software was adopted herein. The convection terms in the governing equations were discretized using the Gauss linear upwind schemes. The SIMPLE algorithm was used for the pressure-velocity coupling.

The rotor motion was tracked by splitting the computational domain into the rotating and stationary parts, and the MRF was taken to integrate these two sub-domains. The MRF method has been commonly used in the simulation of RDTs (Dubas, 2015; Gaggero, 2020; Grümmer, 2016; Song et al., 2015). It is worth noticing that the blades and the rim are the only two components that move with the rotating coordinate system, which is shown in yellow in Figure 2, and that the duct and the far-field boundaries of the computational domain are stationary.

To accommodate non-orthogonal grids, numerical techniques for Laplacian and surface normal gradients were used. Relaxation factors were employed to control the solution convergence. The convergence of the numerical simulation was guaranteed by controlling the iteration residuals to a standard of at least 10-7 for the continuity and momentum variables, indicating that the relative change of the magnitudes between iterations was less than this level.

3.1.1 Turbulence modelling

The CFD method is the unsteady RANS with the k-ω SST turbulence model. The details refer to the article of Lin et al. (2023), which was completed in the framework of this project.

The SST k–ω model is utilized since this turbulence model is able to analyse flows with severe negative pressure gradients in consideration of wall shear (Yao and Davidson, 2019). The SST k–ω turbulence model has been proven by a number of experts to be a promising solution to the hydrodynamic problems of the RDT (Dubas et al., 2015; Gaggero, 2020; Song et al., 2020) and other rotating machinery (Ottersten et al., 2022a; 2022b). The transport equations for turbulent kinetic energy (k) and turbulence dissipation rate (ω) are referred to the research of Menter et al. (2003) and Lin et al. (2020).

3.1.2 Numerical setup

The whole computational domain has a cylindrical shape with a diameter of 10 D_b and a length of 15 D_b, as shown in Figure 3. Here D_b is the blade diameter. The domain inlet is placed at 5 D_b from the front surface of the hubless RDT configuration, and the domain outlet at 10 D_b downstream that surface. These parameters of the dimensions of the computational domain were verified according to the previous work of Grümmer et al. (2017).

The surfaces of the hubless RDT configuration is set with the no-slip wall condition. The inlet boundary of the computational domain is set with the velocity inlet condition, and the outlet boundary with the pressure outlet. The far field boundary of the computational domain is set with the symmetry condition.

As the MRF is used to integrate the rotating and stationary subdomains, the initial rotation coordinate system overlaps with the stationary coordinate system. The coordinate origin is located at the geometric center of the RDT; the coordinate axes directions can be seen in Figure 3; and the rotation axis of the motion coordinate system is the x-axis.

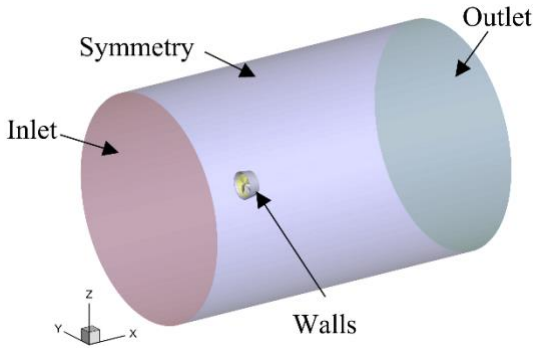

Figure 3. Computational domain and boundary conditions.

The commercial software Pointwise was used to generate the unstructured mesh in the computational domain. Grid cell types include tetrahedrons, pyramids, and hexahedrons. Prism layers are generated near the walls of the hubless RDT, tetrahedrons in the region relatively far away from the walls, and pyramids and hexahedrons for transitions at high skewness locations.

It is critical to enhance simulation accuracy by refining certain regions in the computational domain. To be more specific, the mesh is gradually refined from the RDT walls, where the flow field is more disrupted, to the far field. And the cell growth ratio is 1.2. Furthermore, extra mesh refinement within the gap is necessary because the focus of this study is on the flow condition of the gap, as shown in Figure 4.

The dimensionless wall distance of the first-layer cells, y+, is kept approximately one. The number of grid cell layers in the gap is 22. The checkMesh command in OpenFOAM was used to evaluate the mesh quality, and no warnings and errors were reported for the generated meshes. The maximum aspect ratio is 48.111, and the maximum skewness is 2.566.

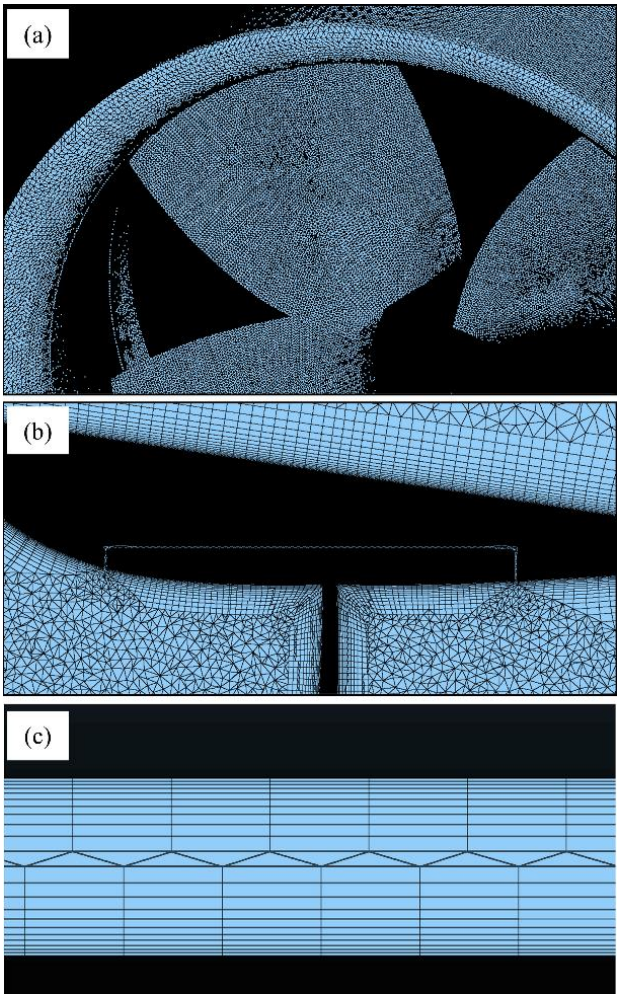

Figure 4. Mesh distribution: (a) surface mesh, (b) boundary layer, and (c) cells in the gap.

3.1.3 Validation of numerical method

The results of the convergence analysis of the generated meshes are listed in Table 2. The convergence analysis is performed at $J = 0.5$, $n = 7.5$ rps, and $\theta = 90°$. The accuracy of the simulations is evaluated by comparing the results of three meshes (approximately 8, 12, and 18 million cells) based on K_T and K_Q. The grid convergence index (GCI) method developed by Celik et al. (2008) is adopted to assess the discretization error of the RDT thrust and torque. The refinement ratio of the grid is adopted as $\sqrt{2}$. The findings reveal that the GCI values of the fine grid are lower than those of the medium grid for both thrust and torque, demonstrating that the numerical uncertainty decreases as the grid is refined. The largest numerical

uncertainty is claimed to be within 3.09% and 1.04% for the medium and fine grids, respectively. The fine grid is utilized as the final grid in this investigation based on the grid convergence analysis.

Table 2. Results of the grid convergence analysis.

	Total number of cells (millions)	K_T	GCI (%)	$10K_Q$	GCI (%)
Coarse	8	0.243	–	0.468	–
Medium	12	0.249	3.09	0.479	2.94
Fine	18	0.251	1.00	0.475	1.04

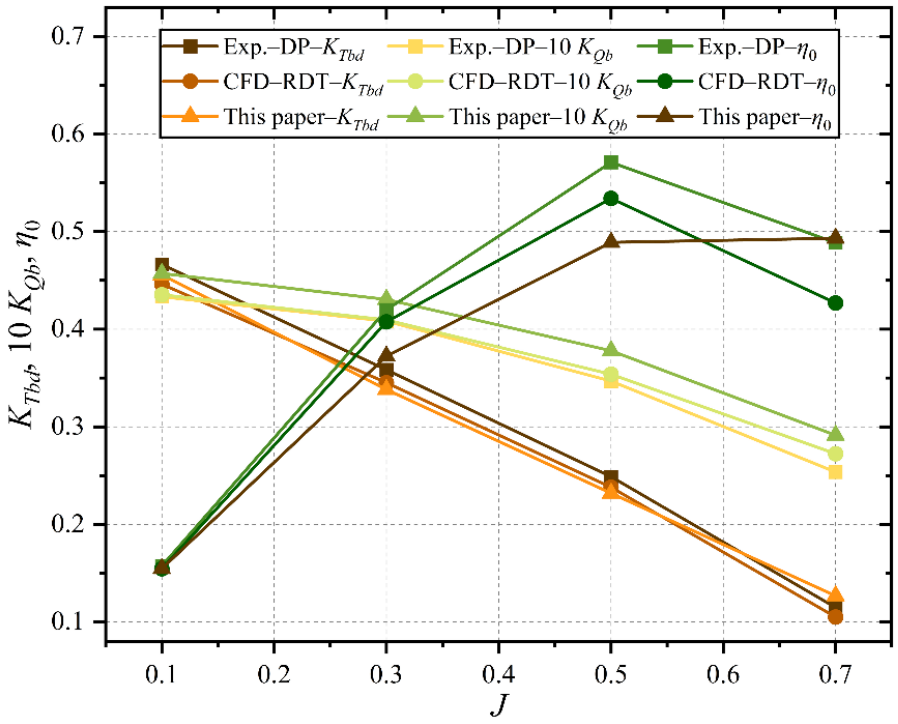

Figure 5. Comparison of open water characteristics between CFD and experimental results.

4 Results

4.1 Comparison to similar benchmark configurations

Since there is a lack of systematic and comprehensive experimental results for the RDT used in this work, a similar result was used for comparison. CFD results for the same RDT but without considering the gap can be obtained from the literature (Song et al., 2020). Experimental results for a similar ducted propeller (DP) with the same MARIN 19A duct and Ka 4-70 propeller can be acquired from the publication (Baltazar et al., 2012). The experimental and numerical simulation results of the open water characteristics with and without considering a gap are compared as

shown in Figure 5. The hydrodynamic coefficients for the comparison are the thrust coefficients of the blade and duct (K_{Tbd}), the torque coefficients of the blade (K_{Qb}), and the efficiency without considering the rim (η_0), respectively. When observing the thrust coefficient, a good consistency is noticed, which confirms the simulation code and the correct use of the blade and duct geometry selection. When comparing the torque coefficient results, a resembling trend can be noticed. The torque calculated by this study is overestimated over the whole range of advance coefficients. This bias is thought to be the result of comparative literatures not taking friction between the duct and the rim into account. In this situation, the overestimation of torque leads to low efficiency. The open water efficiency considering the gap is reduced by around 8% compared to the result without the gap. In addition, similar findings can be observed in the study of Liu and Vanierschot (2021). The efficiency of their numerical simulation of the RDT is about 15% lower than the experimental value of the DP at the high advance coefficient.

4.2 Effects of clearance geometry

4.2.1 Fixed axial segment length of the gap–L_1Text text

In this section, the gap oblique angles (θ) are selected at 15° intervals for numerical analysis to comprehensively investigate the effects of different positions of the inlet and outlet of the gap on the hydrodynamic performance of the RDT. The primary conditions of the numerical simulation are set: $J = 0.5$, $n = 7.5$ rps, and $L_1 = 0.066$ m. Figure 6 shows the hydrodynamic characteristics of the RDT at different θ with a fixed axial segment length of the gap. The individual hydrodynamic coefficients at different θ are normalized based on data at $\theta = 90°$. It is clear that the η reduces gradually as θ grows. The K_T of RDT increases at $\theta = 135^\circ$, but the K_Q rises even more, which leads to a decrease in η instead. Through specifically examining the individual components of thrust and torque, it can be seen that as θ grows, all of the blade thrust coefficients (K_{Tb}), rim thrust coefficients (K_{Tr}), blade torque coefficients (K_{Qb}), and rim torque coefficients (K_{Qr}) increase while all of the duct thrust coefficients (K_{Td}) decrease. It is caused by the fact that as θ grows, the rim expands and the duct contracts.

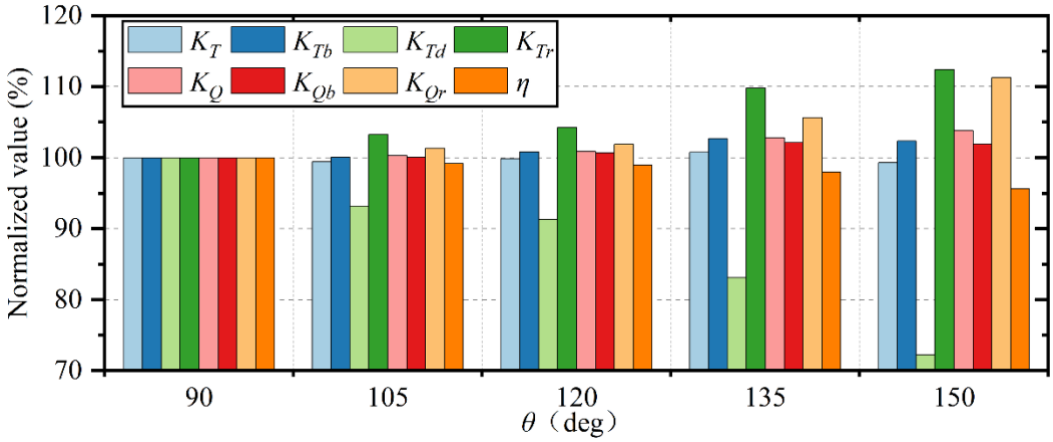

Figure 6. Hydrodynamic characteristics of the RDT at different oblique angles (θ) with a fixed axial segment length of the gap.

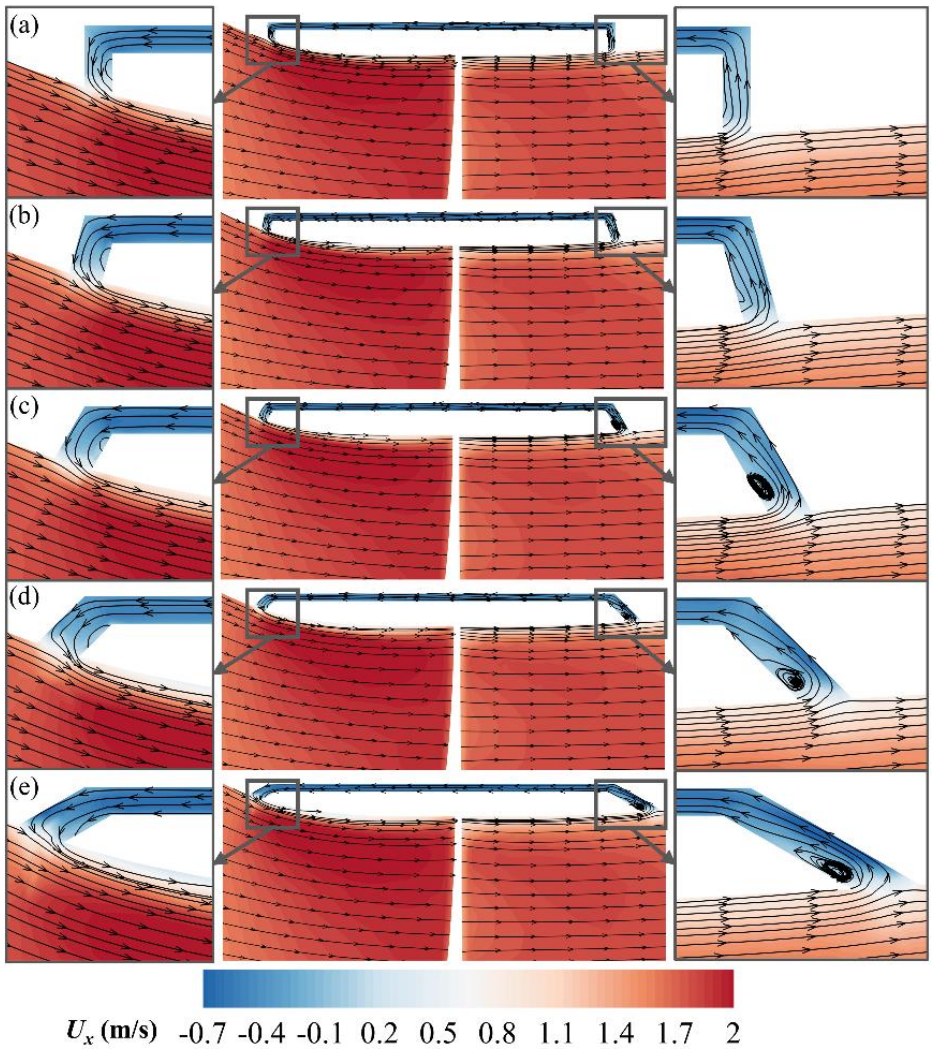

Figure 7. The axial velocity distribution of the flow field at different oblique angles (θ) with a fixed axial segment length of the gap: (a) θ = 90°, (b) θ = 105°, (c) θ = 120°, (d) θ = 135°, and (e) θ = 150°.

Figure 7 illustrates the axial velocity (U_x) distribution of the flow field at different θ with a fixed axial segment length of the gap. It can be observed that the flow direction in the gap is the opposite to the incoming flow direction. This can be expressed as a higher pressure at the downstream gap opening than at the upstream gap opening because the main flow is pressurized by the rotating blades, as shown in Figure 8. It is worth noting that the inlet of the gap flow is on the pressure side behind the blade and the outlet is on the suction side in front of the blade. It leads to a higher relative pressure at the inlet of the gap than at the outlet. The variation of θ changes not only the total length of the gap but also the inlet and outlet positions of the gap. As the inlet position of the gap moves toward the trailing edge of the duct, a small vortex gradually forms at the inlet of the gap. This could be one of the reasons for the reduced efficiency, which will be further analysed in Section 3.2. At the outlet of the gap, the flow in the gap is carried by the incoming flow with higher velocity and merged to increase the stream velocity in front of the blade.

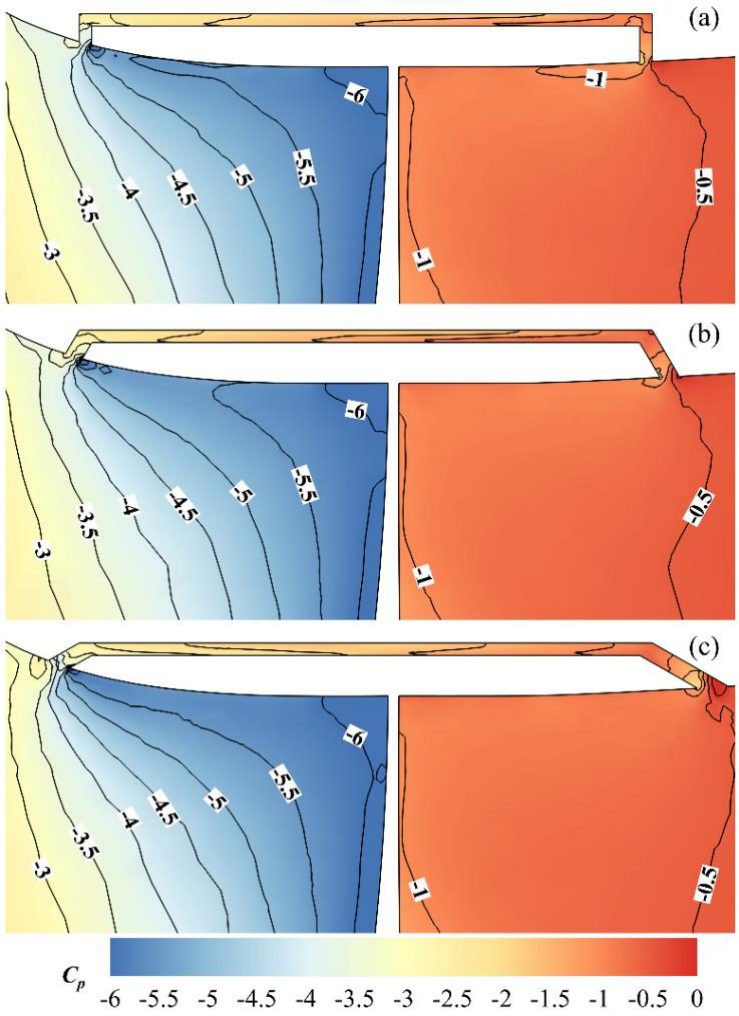

Figure 8. The pressure distribution of the flow field at different oblique angles (θ) with a fixed axial segment length of the gap: (a) $\theta = 90°$, (b) $\theta = 120°$, and (c) $\theta = 150°$.

As shown in Figure 8, the increasing flow velocity at the gap outlet leads to a change in the pressure coefficient ($C_p = P/(0.5\rho V_a^2)$) distribution near here. It further changes the distribution of pressure on the propeller surface, which has an effect on the thrust and torque of the propeller. The position of the gap inlet moves downstream as θ increases, and the pressure at the gap inlet increases gradually.

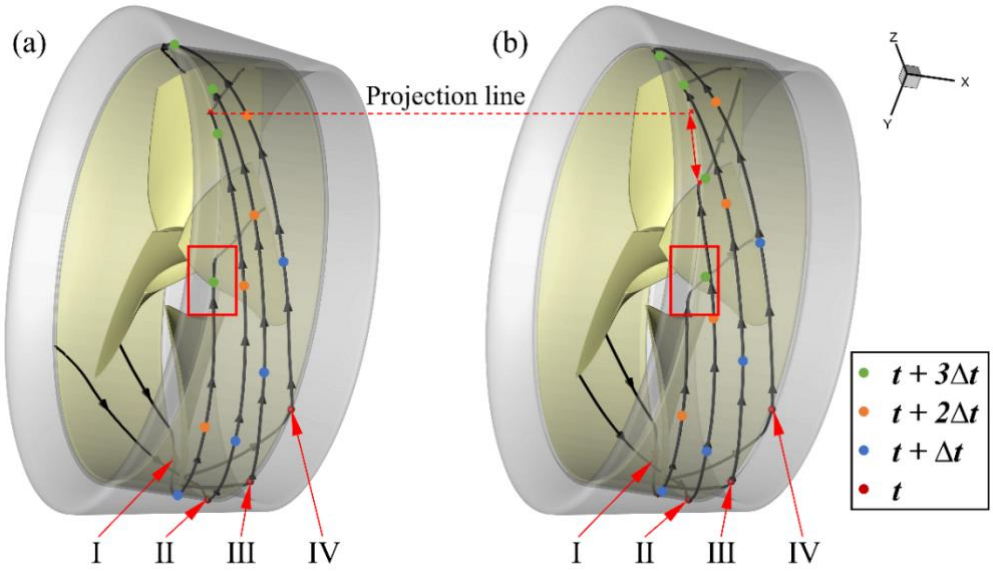

Figure 9. 3D pathlines in the gap at different oblique angles (θ) with a fixed axial segment length of the gap: (a) $\theta = 90°$, and (b) $\theta = 120°$.

Figure 9 shows 3D pathlines in the gap at different θ with a fixed axial segment length of the gap. For a presentation purpose, only the pathlines passing through four feature points (I, II, III, and IV) are plotted. The four points are uniformly distributed at 30° intervals and are located at the inlet of the gap. The fluid particles at the four points were marked at an initial physical time (t) based on the Lagrangian method. The trajectories of these fluid particles were drawn with the time interval (Δt).

As can be seen in Figure 9, the flow is affected by the rotational motion of the propeller and enters the gap with an oblique angle at the entrance. The flow is maintained in the gap in an inclined direction, then exits the gap and is deflected by both the incoming flow and the propeller rotation. It is known that the greater the distance the fluid particles move in the same Δt on the unidirectional pathline, the faster the velocity. When the fluid particles I at $t + 3\Delta t$ are compared in Figures 9a and 9b, it can be seen that the fluid particle with $\theta = 90°$ is still inside the gap, whereas the fluid particle with $\theta = 120°$ has already escaped.

Comparing the trajectories of fluid particles II at the gap outlet, it is observed that the fluid particle with $\theta = 120°$ leaves the gap earlier than the one with $\theta = 90°$, and the relative angle between the gap outlet and the inlet is smaller when $\theta = 120°$.

This indicates that increasing θ reduces the decelerating effect of the gap corner on the particles, that is, increasing θ is beneficial to the development of the gap flow.

4.2.2 Fixed distance between the gap inlet and outlet–L_2

Because adjusting the gap inlet and outlet positions does not result in a significant gain in RDT efficiency, this part expands on the previous section by varying the oblique angle and gap axial segment length under the constraint of fixed distance between the gap inlet and outlet. The primary conditions of the numerical simulation are set: J = 0.5, n = 7.5 rps, and L_2 = 0.066 m. Figure 10 illustrates the hydrodynamic characteristics of the RDT at different θ with the fixed distance between the gap inlet and outlet. The improvement in the RDT efficiency can be demonstrated under all working conditions except the maximum angle of 150°. When θ = 150°, both K_T and K_Q enhances, but K_Q enlarges more, resulting in poor efficiency. When θ reaches 120° and 135°, it is accompanied by an increase in K_Q, although K_T increases significantly. The rise in K_T and the drop in K_Q are only obtained when θ is equal to 105°, but the efficiency gain is limited. The maximum efficiency gain occurs at θ = 135°, which is about 1%. At this point, the K_T increases by approximately 2.6%. The development in θ minimizes the size of the rim, resulting in a reduction in both K_{Tr} and K_{Qr}. It is logical to expect K_{Td} to rise as θ increases, yet it has a tendency to rise and then fall. This phenomenon deserves further discussion in this work.

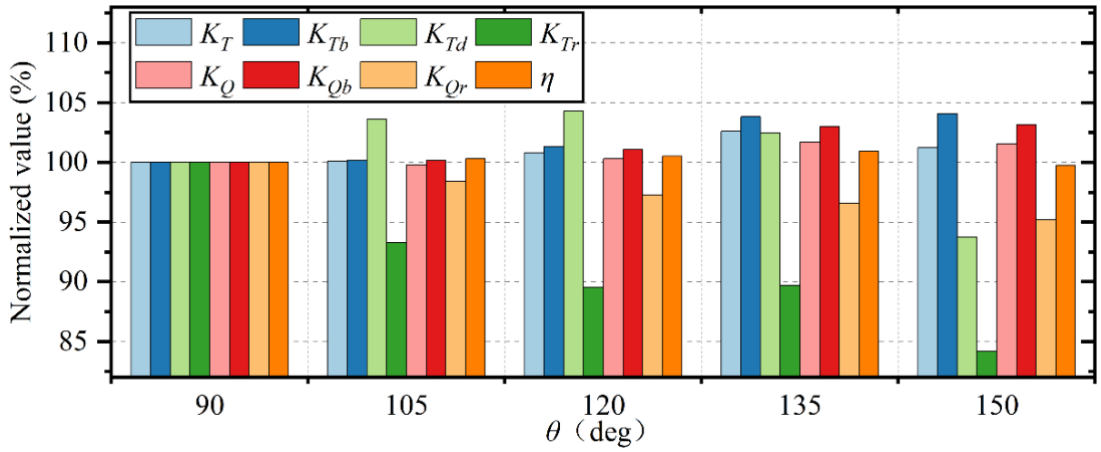

Figure 10. Hydrodynamic characteristics of the RDT at different oblique angles (θ) with the fixed distance between the gap inlet and outlet.

The axial velocity distribution of the flow field at different θ with the fixed distance between the gap inlet and outlet is presented in Figure 11. Compared with Figure 6, after fixing the inlet and outlet positions of the gap, no small vortex is generated at the entrance of the gap for different θ. The initial inlet and outlet locations of the gap were confirmed to be reasonable.

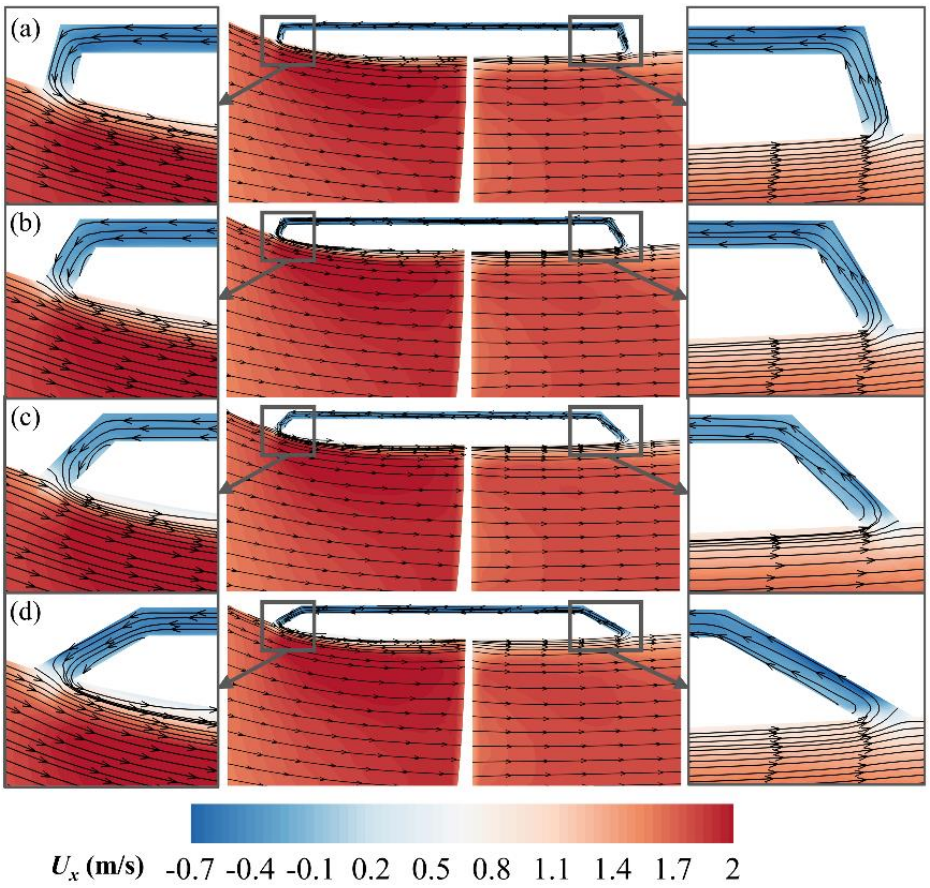

Figure 11. The axial velocity distribution of the flow field at different oblique angles (θ) with the fixed distance between the gap inlet and outlet: (a) θ = 105°, (b) θ = 120°, (c) θ = 135°, and (d) θ = 150°.

To further observe the effect of the gap on the flow near the propeller, three cross sections, named section A, B, and C, were cut at the midpoints of the gap outlet (x/D_b = -0.151), the propeller disk (x/D_b = 0), and the gap inlet (x/D_b = 0.119), as shown in Figure 2. Figure 12 displays the axial velocities distribution in the three cross sections at different θ with the fixed distance between the gap inlet and outlet. As a result of the rotation of the blades, there is a certain phase difference in the flow field characteristics of the three cross sections. It is found that the modification of the gap shape influences the axial velocity distribution in sections A and C, while the effect of the gap is difficult to observe in section B owing to the dominance of the rotational motion of the blade. The presence of the gap expands the axial flow rate near the rim, as shown in cross section A. The shedding vortex was observed at the blade tip of the RDT, as shown in cross section C.

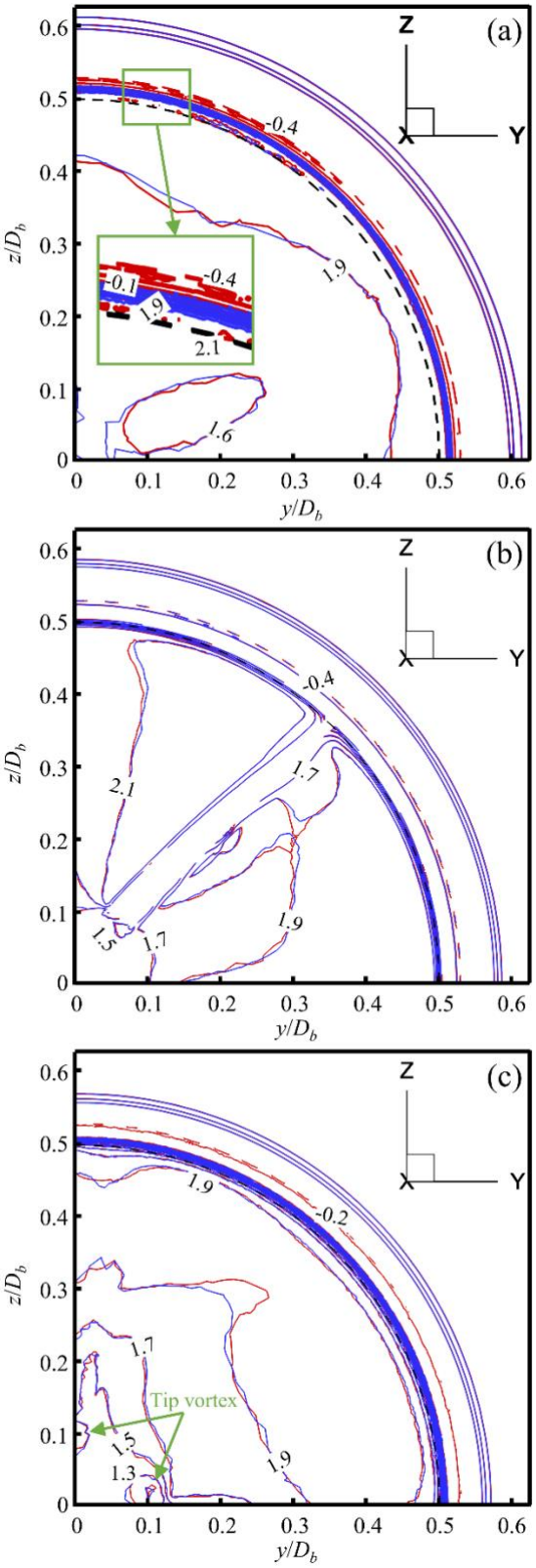

Figure 12. The dimensionless axial velocity contour distribution at different oblique angles ($\theta = 90°$ colored by red and $\theta = 135°$ colored by blue) with the fixed distance between the gap inlet and outlet: (a) cross section A, (b) cross section B, and (c) cross section C.

The vorticity distribution in the wake field at different θ is illustrated in Figure 13. The vortex generated by the blade tip of RDT is well observed and verified. Vortices shedding from the gap and developing along the inner side of the duct to the wake are also observed. Nonetheless, the differences between the two different θ are very limited. This reflects that the gap oblique angle change has a limited effect on the downstream wake development.

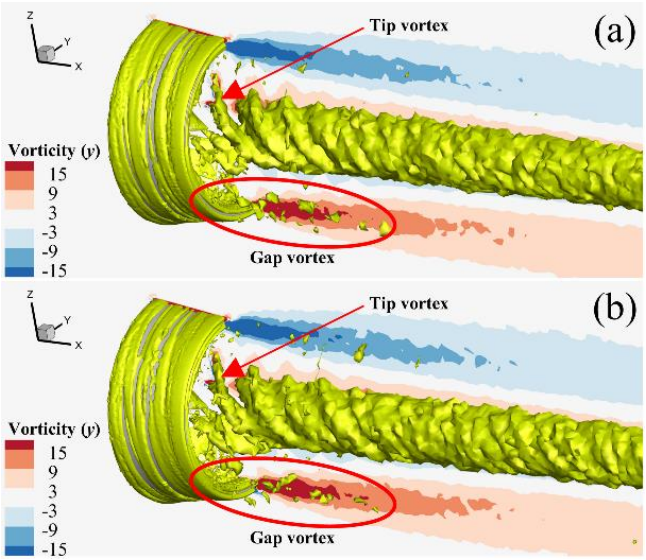

Figure 13. Vortex distribution visualized with an isosurface of the instantaneous Q-criterion in the wake field for the fixed inlet and outlet positions of the gap with different corner angles: (a) θ = 90°, and (b) θ = 135°.

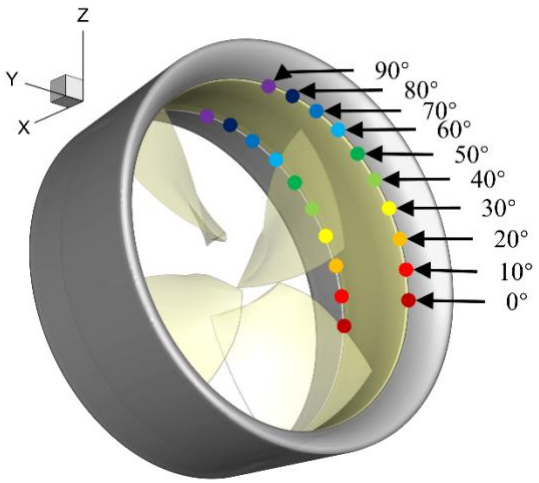

Figure 14. Positions and angles of the monitoring points located at the quarter-gap inlet and outlet.

Subsequently, the impacts of different gap shapes are compared by quantitatively analyzing the pressure and velocity variation at the gap inlet and outlet. The locations and angles (φ) of the monitoring points located at the quarter-gap inlet and outlet are displayed in Figure 14.

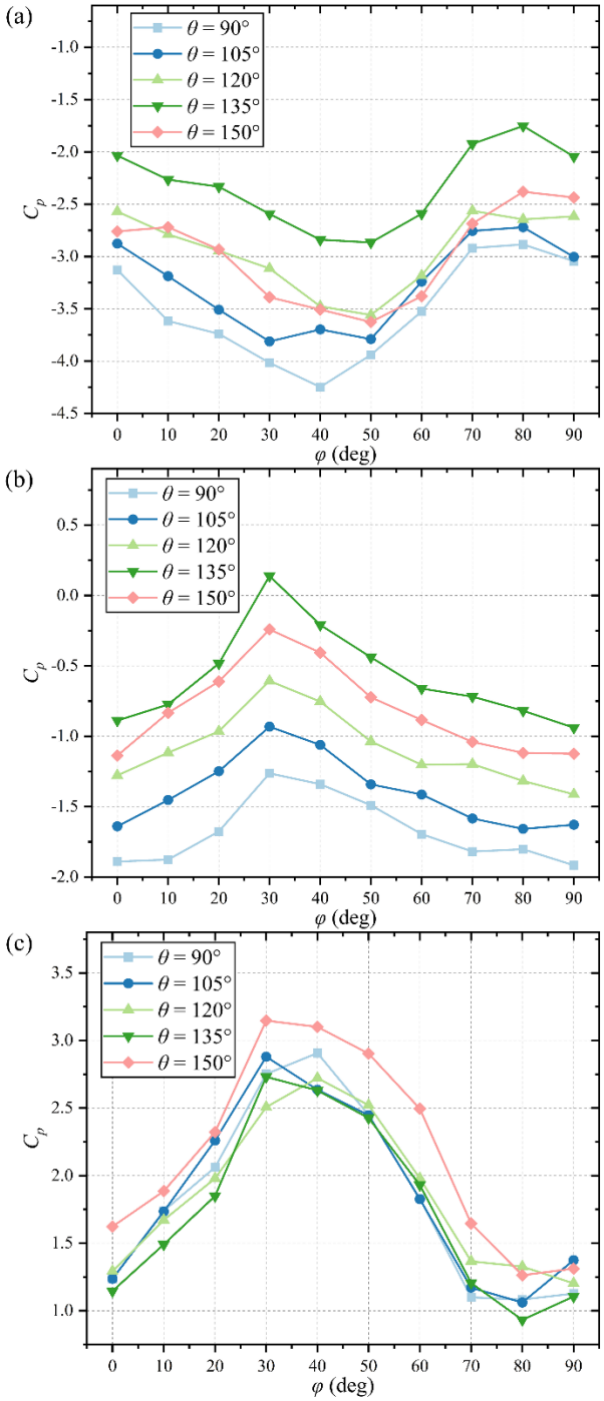

Figure 15. Pressure coefficient (C_p) curves at different monitoring points at different oblique angles (θ) with the fixed distance between the gap inlet and outlet: (a) C_p of the gap outlet, (b) C_p of the gap inlet, and (c) relative C_p between the inlet and outlet of the gap.

Figure 15 depicts the C_p of the gap inlet and outlet as well as the relative C_p of the two. The varying trends of C_p at different θ are found to be consistent. At the gap outlet, C_p decreases and then increases, reaching the minimum value at the middle of the blade (φ is equal to approximately 45°). At the gap inlet, C_p grows first and then drops, reaching a maximum at φ = 30°. Since the relative pressure coefficient is the difference between the inlet and outlet, it satisfies the law of first increasing and then decreasing. As can be observed in Figures 15a and 15b, the C_p at both the gap outlet and inlet grows with increasing θ and decreases beyond θ = 135°. This is in agreement with the trend of efficiency variation of the RDT (see Figure 10), indicating that the change of the gap shape on the pressure is one of the causes of the efficiency variation. As can be noticed in Figure 15c, the relative C_p is lowest at θ = 135° and largest at θ = 150°. This suggests that reducing the relative pressure at the gap inlet and outlet is beneficial for improving the efficiency of the RDT.

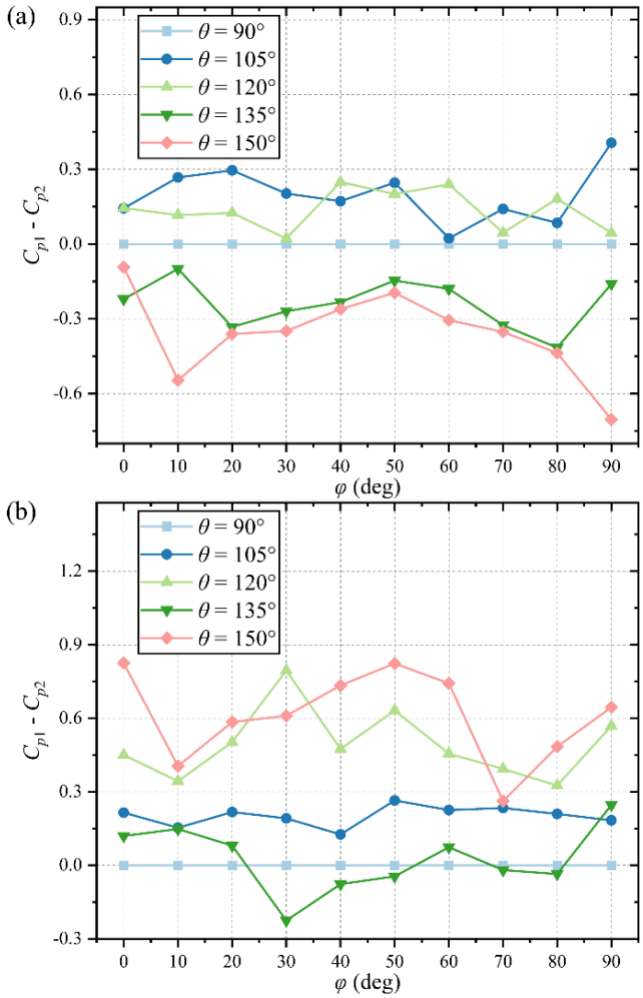

Figure 16. Value of the difference in pressure coefficients for the results of fixed L_1 (C_{P1}) and fixed L_2 (C_{P2}) at different monitoring points at different oblique angles (θ): (a) the gap outlet, and (b) the gap inlet.

Figure 16 compares the value of the difference in pressure coefficients for the results of fixed L_1 (C_{P1}) and fixed L_2 (C_{P2}) at different φ and θ. When $\theta = 90°$, the geometric model is the same, leading to $C_{P1} = C_{P2}$. At the gap outlet, C_{P1} is greater than C_{P2} when θ is equal to 105° and 120°, while the opposite is true when the θ increases. At the gap inlet, C_{P1} is always larger than C_{P2} except when $\theta = 135°$. The results show that varying the position of the gap inlet and outlet has a significant influence on the pressure distribution when θ is the same.

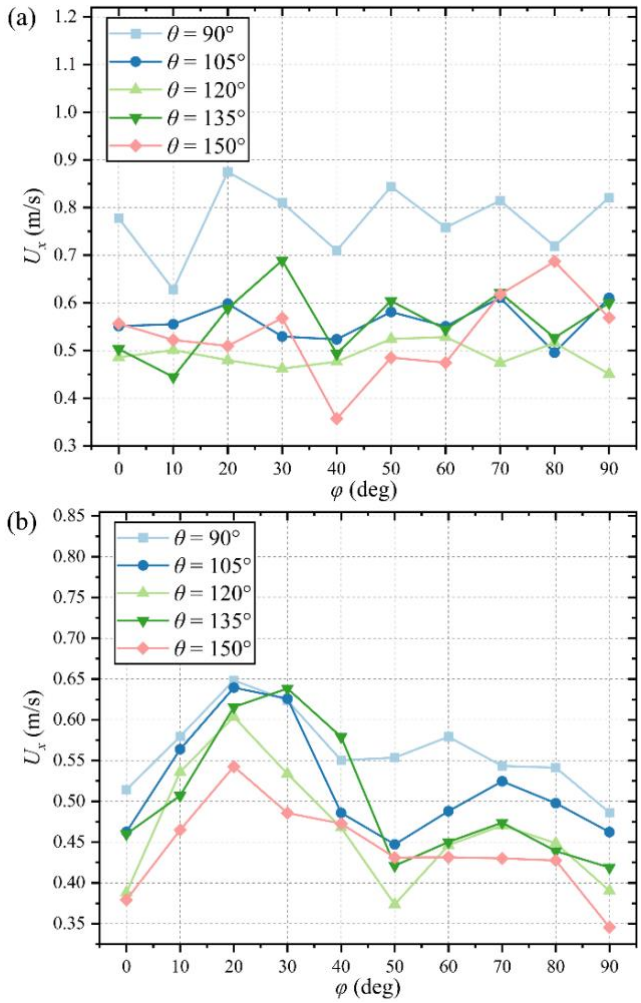

Figure 17. Axial velocities (U_x) of different monitoring points at different oblique angles (θ) with the fixed distance between the gap inlet and outlet: (a) U_x of the gap outlet, and (b) U_x of the gap inlet.

Figure 17 and Figure 18 demonstrates the flow velocities of different monitoring points at different θ with the fixed distance between the gap inlet and outlet. It is shown that the flow velocities at the gap outlet located in front of the blade is almost unaffected by the propeller rotational flow, while the flow velocities at the gap inlet located behind the blade shows a tendency to rise and then fall.

Modifying the gap shape significantly reduces the U_x at the gap outlet, as shown in Figure 17a. When $\theta = 150°$, the U_x curve fluctuates the most, representing the greatest nonuniformity in the flow velocity, which is one of the reasons for the reduced efficiency of this gap shape. The variation pattern of the combined velocity ($U_{yz} = \sqrt{U_y^2 + U_z^2}$) at θ on cross sections is the opposite of that of K_Q, as shown in Figure 18a and Figure 10. When $\theta = 105°$, U_{yz} is the largest and K_Q is the smallest. As a result, it is suggested that the U_{yz} be increased at the gap outlet in order to reduce the RDT torque.

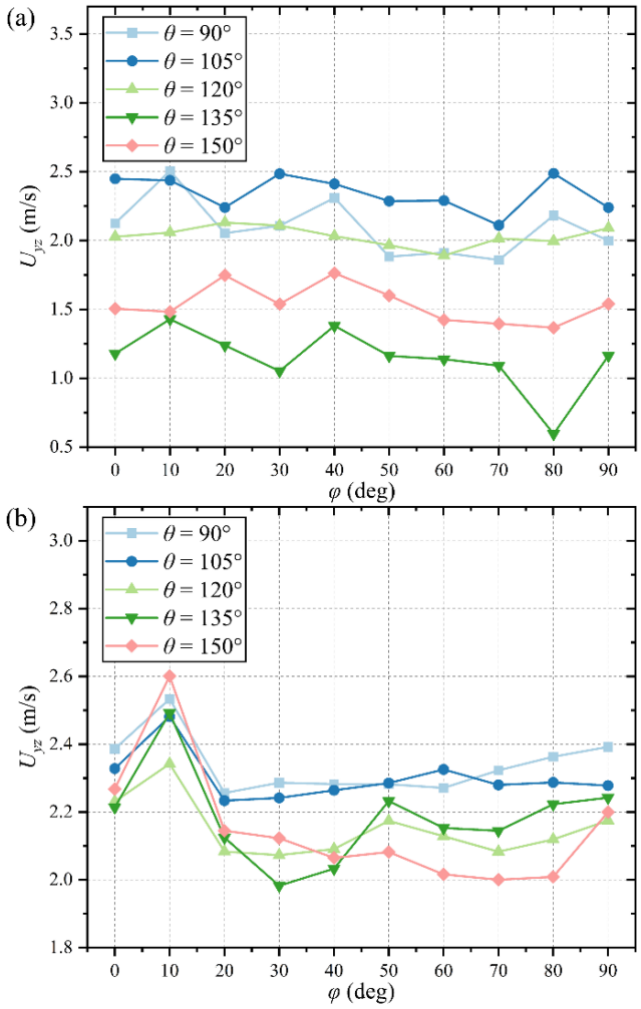

Figure 18. Combined velocities (U_{yz}) of different monitoring points on cross sections at different oblique angles (θ) with the fixed distance between the gap inlet and outlet: (a) U_{yz} of the gap outlet, and (b) U_{yz} of the gap inlet.

5 Other reports

Two scientific publications were produced based on the results of this project: one journal paper, and one preprint. The journal one presented the novel approach of improving the clearance geometry to increase hydrodynamic efficiency, as shown below.

- Lin J., Yao H.-D., Wang C., Su Y., Yang C., Hydrodynamic performance of a rim-driven thruster improved with gap geometry adjustment, Engineering Applications of Computational Fluid Mechanics, 17(1), 2183902, 2023. DOI: https://doi.org/10.1080/19942060.2023.2183902 (Journal IF: 6.519)

The preprint reported the investigation of a fluid-structure interaction (FSI) solver implemented on ANSYS. A benchmark FSI case was proposed to validate the solver. This paper is a preprint and has been under review in a journal. A strongly coupled FSI approach was adopted to couple a CFD solver and an FEA solver. In addition, the CFD and the FEA were performed separately. The dynamics of vortex-induced vibration was analysed using the developed method.

- Aravindhan Venkatesh, Huadong Yao, Xiao Xue, and Jiqiang Niu. Vortex-induced vibrations of a deformable splitter plate behind a square cylinder controlled by active pitch oscillation. engrXiv.
  DOI: https://doi.org/10.31224/3165 (preprint)

One master's thesis project, supported by Erasmus+ of the EU's programme, was carried out within the framework of this project. It is listed as follows.

- Asci A.B., Design and Simulation of Electric Rim-Driven Hubless Propeller, Chalmers University of Technology, 2022.

6 Summary

In this project, a new way of improving the hydrodynamic efficiency of the hubless RDT was demonstrated. That is, modifying the gap inlet and outlet oblique angles was explored. Given the volume of the project, numerical simulations were used to clarify the mechanism of the gap flow. The numerical tools is the open-source software OpenFOAM.

In the gap, the flow direction is the inverse of the incoming flow direction. The flow enters the gap obliquely from the entrance and is kept inclined in the gap. The increasing flow velocity at the gap outlet has an effect on the thrust and torque of the propeller.

Under the condition of fixed gap axial length, the inlet and outlet positions of the gap are altered by enlarging the oblique angle of the gap inlet and outlet, but the hydrodynamic efficiency is not improved. Increasing the oblique angle reduces the corner's deceleration effect on the flow.

When the inlet and outlet positions of the gap are fixed, increasing the oblique angle of the gap inlet and outlet leads to the improvement of the efficiency. In comparison to the baseline model with the oblique angle of 90°, the new gap designs with the oblique angle from 105° to 135° result in an increase of the efficiency. At the oblique angle of 135°, the maximum efficiency increase of about 1% is achieved.

Reducing the relative pressure at the gap inlet and outlet is beneficial to increasing the efficiency. One of the causes of the efficiency variation is the change in pressure due to gap shape modification. Another reason for the reduced efficiency is nonuniformity in the flow velocity at the gap outlet.

As notice in the present project, the transient hydrodynamics of the hubless RDT with the gap flow considered is a challenging engineering and research and engineering topic. To investigate further, analyzing the fluid-solid coupling for the blade vibration, ship-propulsor interference, cavitation, and noise will be necessary. In addition, it is desirable to carry out experimental research on the model-scale and full-scale RDT.

7 Acknowledgements

The computations/data handling were enabled by resources provided by the Swedish National Infrastructure for Computing (SNIC) at Tetralith, partially funded by the Swedish Research Council through grant agreement no. 2018-05973. We thank all support technicians at Tetralith for their assistance, which was made possible through application support provided by SNIC.

8 References

Adler, G.A., Design and system integration of a rim jet solution utilizing DFMA. Master's thesis, KTH, 2020.

Andersen, T. P., Design of rim driven waterjet pump for small rescue vessel. Master's thesis, Chalmers University of Technology, 2014.

Baltazar, J., Falcão de Campos, J. A. C., & Bosschers, J., Open-water thrust and torque predictions of a ducted propeller system with a panel method. International Journal of Rotating Machinery, 2012, 1–10. https://doi.org/10.1155/2012/474785

Bang D., Polinder H., Shrestha G., Ferreira J.A., European Wind Energy Conference, 2008, pp. 1-7.

Cai, M., Yang, C., Wu, S., Zhu, Y., and Xie, Y., "Hydrodynamic analysis of a rim-driven thruster based on RANS method," OCEANS 2015 - MTS/IEEE Washington, 2015, pp. 1-5.

Cao, Q., Hong, F., Tang, D., Hu, F., Lu, L., Prediction of loading distribution and hydrodynamic measurements for propeller blades in a rim driven thruster, Journal of Hydrodynamics, Ser. B, 24(1): 50-57, 2012.

Cao, Q., Hong, F., Tang, D., Hu, F., & Lu, L. Prediction of loading distribution and hydrodynamic measurements for propeller blades in a rim driven thruster. Journal of Hydrodynamics, 24(1), 50–57, 2012. https://doi.org/10.1016/S1001-6058(11)60218-7

Cao, Q., Wei, X., Tang, D., & Hong, F. Study of gap flow effects on performance of rim driver thrusters. In Proceedings of the 13th National Conference on Hydrodynamics and the 26th National Symposium on Hydrodynamics, Tsingtao, China, 1197–1206, 2014.

Celik, I. B., Ghia, U., Roache, P. J., & Freitas, C. J. Procedure for estimation and reporting of uncertainty due to discretization in CFD applications. Journal of Fluids Engineering–Transactions of the ASME, 130(7), 078001, 2008.

Dubas, A. J., Bressloff, N. W., & Sharkh, S. M. Numerical modelling of rotor–stator interaction in rim driven thrusters. Ocean engineering, 106, 281–288, 2015. https://doi.org/10.1016/j.oceaneng.2015.07.012

Drouen L., Charpentier J. F., Hauville F., Semail E., and Clenet S., A coupled electromagnetic / hydrodynamic model for the design of an integrated rim-driven naval propulsion system," in Proc. ElectrIMACS, Montreal, QC, Canada, Jun. 2008, pp. 1–6.

Gaggero, S. Numerical design of a RIM-driven thruster using a RANS-based optimization approach. Applied Ocean Research, 94, 101941, 2020. https://doi.org/10.1016/j.apor.2019.101941

Grümmer, H. Design and Optimization of a Hubless rim-driven Thruster for an Autonomous Surface Vehicle using RANSE Simulation, master's dissertation, Technical University of Berlin, German, 2016.

Grümmer, H., Harries, S., & Hochbaum, A.C. Simulation-driven Design of a Rim Drive for an Autonomous Vehicle. In Fifth International Symposium on Marine Propulsors, Espoo, Finland. 2017

Jiang, H., Ouyang, W., Sheng, C., Lan, J., & Bucknall, R., Numerical investigation on hydrodynamic performance of a novel shaftless rim-driven counter-rotating thruster considering gap fluid. Applied Ocean Research, 118, 102967, 2022 https://doi.org/10.1016/j.apor.2021.102967

Konsberg Maritime, Permanent Magnet tunnel thruster TT-PM 1600 - Kongsberg Maritime, https://www.kongsberg.com/zh-hans/maritime/products/propulsors-and-propulsion-systems/thrusters/tunnel-thrusters/permanent-magnet-tunnel-thruster-tt-pm/tt-pm-1600/

Kort, L., Elektrisch angertriebene schiffsschraube. German Patent, 688, 13, 1940

Lea, M., Thompson, D., Van Blarcom, B., Eaton J., Friesch, J., Richards, J., Scale model testing of a commercial rim driven propulsor pod. Journal of Ship Production, 19 (2), 121–130, 2003

Li Y, Song B, Mao Z, Tian W. Analysis and Optimization of the Electromagnetic Performance of a Novel Stator Modular Ring Drive Thruster Motor. Energies. 2018; 11(6):1598.

Lin, J., Zhao, D., Guo, C., Zhang, Z., & Su, Y. Numerically modeling the effect of flexibility on flow around marine engineering structures: Using the shape of the Saguaro Cactus. Journal of Coastal Research, 36(3), 628–635., 2020. https://doi.org/10.2112/JCOASTRES-D-19-00115.1

Lin J., Yao H.-D., Han Y., Su Y., Zhang C. Shape optimization and hydrodynamic simulation of a Magnus anti-rolling device based on fully parametric modeling. Physics of Fluids, 35 (5): 055136. 2023. DOI: https://doi.org/10.1063/5.0152179

Lin J., Yao H.-D., Wang C., Su Y., Yang C., Hydrodynamic performance of a rim-driven thruster improved with gap geometry adjustment, Engineering Applications of Computational Fluid Mechanics, 17(1), 2183902, 2023. DOI: https://doi.org/10.1080/19942060.2023.2183902

Liu, B., & Vanierschot, M. Numerical study of the hydrodynamic characteristics comparison between a ducted propeller and a rim-driven thruster. Applied Sciences, 11(11), 4919. 2021. https://doi.org/10.3390/app11114919

Liu, B., Vanierschot, M., & Buysschaert, F. Comparison study of the $k - kL - \omega$ and $\gamma - Re\theta$ transition models in the open water performance prediction of a

rim-driven thruster. In Conference on Modelling Fluid Flow (CMFF'22), Budapest, Hungary, 70–77. 2022a, August.

Liu, B., Vanierschot, M., & Buysschaert, F., Effects of transition turbulence modeling on the hydrodynamic performance prediction of a rim-driven thruster under different duct designs. Ocean Engineering, 256, 111142. 2022b. https://doi.org/10.1016/j.oceaneng.2022.111142

Menter, F. R., Kuntz, M., & Langtry, R. Ten years of industrial experience with the SST turbulence model. Turbulence, heat and mass transfer, 4(1), 625–632, 2003.

Ottersten, M., Yao, H., & Davidson, L. Inlet gap effect on aerodynamics and tonal noise generation of a voluteless centrifugal fan. Journal of Sound and Vibration, 540(8), 117304, 2022a. https://doi.org/10.1016/j.jsv.2022.117304

Ottersten, M., Yao, H., & Davidson, L. Inlet gap influence on low-frequency flow unsteadiness in a centrifugal fan. Aerospace, 9(12), 846, 2022b. https://doi.org/10.3390/aerospace9120846

Santiago, P.S., Rim-Jet - A Mechanical Design for a Shaftless Propulsor, Master's thesis, KTH, 2019.

Song, B.W.; Wang, Y.J.; Tian, W.L. Open water performance comparison between hub-type and hubless rim driven thrusters based on CFD method. Ocean Eng. 2015, 103, 55–63.

Song, X., Zhao, G., Yuan, L., Yang, B., Tian G., & Ai X., Numerical research of hydrodynamic performance impact factors of rim-driven thruster. Ship Engineering, 42(7), 67–71, 2020. https://doi.org/10.13788/j.cnki.cbgc.2020.07.13

Tuohy, P., M., Smith, A. C., Husband, M., Induction rim-drive for a marine propulsor. International Conference on Power Electronics, Machines and Drives. (pp.1-6), 2010

Voith, The reference in silent thrusters: Voith rim-drive technology, 2021.

Van der Velden™ Marine Systems, The EPS thruster: a silent revolution in thruster technology, 2006.

Wardell G S. Retractable bow thruster: U.S. Patent 4,294,186[P]. 1981-10-13.

Yamaha Motor, 2020, https://global.yamaha-motor.com/news/2020/0731/harmo.html

Yakovlev, A. Y., Sokolov, M. A., & Marinich, N. V. Numerical design and experimental verification of a rim-driven thruster. In Proceedings of Second International Symposium on Marine Propulsors, Hamburg, Germany, 396–403, 2011, June.

Yan, X., Liang, X., Ouyang, W., Liu, Z., Liu, B., and Lan, J. A review of progress and applications of ship shaft-less rim-driven thrusters. Ocean Engineering, 144:142–156, 2017.

Yao, H., & Davidson, L., Vibro-acoustics response of a simplified glass window excited by the turbulent wake of a quarter-spherocylinder body. The Journal of the Acoustical Society of America, 145(5), 3163–3176, 2019. https://doi.org/10.1121/1.5109548

Yakovlev, A.Y., Sokolov, M.A., Marinich, N.V., Numerical design and experimental verification of a rim-driven thruster, Proceedings of Second International Symposium on Marine Propulsors. Hamburg, Germany. 2011.

Zhai, S., Jin, S. B., Chen, J. Q., Liu, Z. H., & Song, X. L., CFD-based multi-objective optimization of the duct for a rim-driven thruster. Ocean Engineering, 264, 112467, 2022. https://doi.org/10.1016/j.oceaneng.2022.112467

Zhu, Z. P., & Liu, H. L., The external characteristics and inner flow research of rim-driven thruster. Advances in mechanical engineering, 14(2), 2022. https://doi.org/10.1177/16878132221081608

Lighthouse gathers leading maritime stakeholders through a Triple-Helix collaboration comprising industry, society, academies and institutes to promote research, development and innovation within the maritime sector with the following vision:

Lighthouse – for a competitive, sustainable and safe maritime sector with a good working environment

LIGHTHOUSE PARTNERS

CHALMERS · KTH VETENSKAP OCH KONST · Linnéuniversitetet · GÖTEBORGS UNIVERSITET

VÄSTRA GÖTALANDSREGIONEN · SJÖFARTSVERKET · Stiftelsen Sveriges Sjömanshus · SVENSK SJÖFART Swedish Shipowners Association

LIGHTHOUSE ASSOCIATE MEMBERS

BUREAU VERITAS · ivl · RI.SE · SSPA Your Maritime Solution Partner · vti · DNV